Revision 3

Crystal chemistry of synthetic Ti-Mg bearing hibonites: A single crystal X-ray study

Mattia Giannini[1,*], Tiziana Boffa Ballaran[1] and Falko Langenhorst[2]

[1]*Bayerisches Geoinstitut, University of Bayreuth, D-95440 Bayreuth, Germany*

[2]*Institut für Geowissenschaften, Friedrich-Schiller-Universität Jena, D-07745 Jena, Germany*

[*]*Corresponding author, e-mail: mattia.giannini@uni-bayreuth.de*

Plan of the article:

Abstract:

Hibonite single crystals were synthesized using two different techniques: hot-pressing of polycrystalline hibonite by means of piston-cylinder apparatus and solid state reaction using citrate-based sol-gel precursors. Chemical analyses, UV/Vis spectroscopy and single crystal X-ray characterization were performed on four sets of Ti-Mg bearing hibonites in order to investigate the substitution mechanism of Ti^{3+}, Ti^{4+} and Mg^{2+}, relevant for hibonites found in Calcium-Aluminum-rich inclusions in meteorites. The unit-cell volume of hibonite depends linearly on the concentration of Ti and Mg: $V = 8.21(3) \cdot (Ti_{tot} + Mg)_{a.p.f.u.} + 586.06$ (1). Structural refinements, carried out in the space group $P6_3/mmc$, demonstrate that Ti occupies two sites: M2, a trigonal bipyramid, and M4, a distorted octahedron occurring in face-sharing pairs. The Ti occupancy factor was refined at both sites. Due to the repulsion of neighboring Ti cations the bond distance M4-O3 increases with increasing Ti content and the cations are displaced from the central position of the polyhedron. The displacement factors $M2_{U33}$ and the site occupancy factor for Ti in the M2 site positively correlate for the samples which have more than 0.3–0.4 $Ti_{a.p.f.u.}$, while $M2_{U33}$ remains that of pure hibonite for small Ti occupancies at the M2 site. This plateau of displacement factor reflects the local strain fields around the substituted Ti atoms and its magnitude indicates that these strain fields begin to overlap at a Ti-Ti separation of about 1-2 unit cells. For a sample synthesized at low oxygen fugacity we detected Ti^{3+} by means of UV/Vis absorption spectroscopy. The presence of Ti^{3+} has a clear effect on the M4-M4 distance which deviates from the linear trend

48 described by samples containing mainly Ti^{4+}. The average bond length M3-O depends linearly on
49 the Mg content of these synthetic hibonites clearly indicating that Mg occupies this site.
50
51 **Keywords**:
52 hibonite, X-ray diffraction, single crystal, calcium hexaluminates, titanium
53

INTRODUCTION

Hibonite is a mineral rarely occurring on Earth, where it is mostly found in alluvial deposits as a product of high grade metamorphism from upper amphibolite to granulite facies (Maaskant 1980; Ulianov et al. 2005; Nagashima et al. 2010). In terrestrial systems, the composition of hibonite differs significantly from its end-member $CaAl_{12}O_{19}$ composition, showing major REE substitution; the terrestrial mineral has typically black-brownish to black color. Hibonite is also known in the ceramic industry as calcium hexaluminate ($CaO{\cdot}6Al_2O_3$ or CA_6), where it is used for various applications, for example, as reinforcement fiber in composite material (Cinibulk 1995; An et al. 1996; Dominguez et al. 2001).

Besides its rare natural occurrence hibonite is however of great interest because it is a common constituent of Calcium-Aluminum-rich inclusions (CAIs) in carbonaceous chondrites, providing evidence for the formation of the first solid matter in our solar system. Based on observed ^{26}Mg excess (Hinton et al. 1988; Ireland 1990) and on thermodynamic calculations (Grossman and Clark 1973), hibonite is considered to be a primary condensate from a hot gas of solar composition. It is the second most Al-rich phase usually found in CAIs after corundum (e.g. Simon et al. 2002; Nakamura et al. 2007). Hibonite has attracted a lot of attention over the years due to the fact that it contains significant amounts of Ti, Mg, Fe, Si and V. The transition metals (Ti, Fe, V) have more than one available oxidation state which may be correlated to the redox conditions of the solar nebula during the condensation process (Ihinger and Stolper 1986; Beckett et al. 1988; Doyle et al. 2011; Giannini et al. 2011). However, the structural site at which a cation is accommodated in a material as well as the substitution mechanism in complex systems may often determine the oxidation state independently from the oxygen fugacity. Therefore, determining the Ti site distribution in hibonite and its substitution mechanism is as important as measuring its oxidation state.

So far, hibonite has been characterized by means of single crystal X-ray diffraction only on few terrestrial samples from Madagascar (Bermanec et al. 1996; Hofmeister et al. 2004) and on a gem-quality crystal from Myanmar (Nagashima et al. 2010). To our knowledge there are no reported studies on hibonite single crystals from chondrites, mostly because the typical grain sizes of these crystals (< 30 μm) are not suitable for conventional X-ray diffractometers, as well as due to technical limitations for sample preparation and extraction.

The X-ray structural refinements on the terrestrial samples show that hibonite, $AM_{12}O_{19}$, crystallizes in space group $P6_3/mmc$ (Z = 2). The structure can be described as a stacking of close-packed oxygen layers parallel to the basal plane of the hexagonal cell, forming spinel-like blocks ($S = [M_6O_8]^{2+}$) alternated by hexagonal close-packed blocks ($R = [AM_6O_{11}]^{2-}$) in a sequence that can be written as *S'RSR'S'* where the apex indicates a block rotated with respect to the 2-fold axis parallel to the *c* axis. This arrangement of layers creates a variety of coordination environments, starting from a large 12-fold coordinated site (A) sitting in the *R* blocks and, in the case of hibonite, being mainly occupied by Ca. The M ions are distributed over five different sites: three with octahedral (M1, M4, M5), one with tetrahedral (M3) and one with bipyramidal coordination (M2), as illustrated in Fig. 1 (Bermanec et al. 1996). The atomic site M2 is split into two positions according to a dynamic disorder model and also may be suitable for substitutions of Ti (Nagashima et al. 2010).

Few methods have been able to successfully produce synthetic single crystals of hibonite. Mateika and Laudan (1979) reported the synthesis of a hibonite-like compound ($BaAl_{12}O_{19}$) using the Czochralski method, and this was followed by the growth of pure hibonite single crystals using the traveling solvent floating zone method (Utsunomiya et al.1988). More recently, Hofmeister et al. (2004) obtained pure end-member hibonite by laser-heating pellets of CaO-Al_2O_3 mixtures. Both

techniques, however, are not suitable for controlling the oxygen fugacity during crystal growth, moreover laser heating syntheses are often characterized by non-equilibrium conditions.

In this study we present single crystal X-ray diffraction (XRD) measurements on four sets of Ti-Mg bearing synthetic hibonites prepared, at variable fO_2, with two different techniques: hot-pressing of polycrystalline hibonite by means of piston-cylinder apparatus, and solid state reaction using citrate-based sol-gel precursors. These methods allow synthesis of hibonite single crystals which are good proxies for meteoritic hibonites. Our aim is to provide a better understanding of the site occupancy and substitution mechanism for Ti^{3+}/Ti^{4+}-Mg^{2+}-bearing hibonites and to address the question whether it is possible to differentiate between the role of oxygen fugacity and the structural control on the oxidation state of Ti.

EXPERIMENTAL METHODS

Piston-cylinder

A first attempt to synthesize single crystals of hibonite was done using a piston-cylinder apparatus, as proposed by Geiger et al. (1988). Since these authors used oxide mixtures as starting materials for their experiment, which resulted mostly in unreacted corundum, we have adopted a two-stage synthesis method: polycrystalline hibonite was first synthesized at room pressure and then used as starting material for a high pressure and high temperature experiment employing a piston-cylinder apparatus (Boyd and England 1960) at the Bayerisches Geoinstitut (Table 1). To obtain the polycrystalline starting material, a stoichiometric and homogenized mixture of $CaCO_3$, Al_2O_3, MgO and TiO_2 was decarboxylated up to 900 °C, pressed into a 1/2" pellet and fired in air at 1430 °C for 14 hours. The run product was identified as almost pure hibonite by means of X-ray powder diffraction (XRPD) and it was subsequently sealed inside a Pt capsule, which was inserted into a 1/2" MgO-pyrex assembly equipped with graphite heater. The piston-cylinder experiment was run

at 15 kbar, the temperature was monitored using a type-D (W - 3 %Re / W - 25 %Re) thermocouple and it was kept constant at 1450 °C for 12 h; then temperature was raised to about 2000 °C for 90 min before immediate quench. The Pt capsule partially melted during the experiment. The recovered crystalline material consisted of single crystals of hibonite of up to 200 μm in size and with platy morphology. Due to the graphite heater, the oxygen fugacity for this synthesis can be estimated to have varied between log fO_2 = -7.6 and log fO_2 = -4.9 during the temperature step from 1450 °C to 2000 °C (Jakobsson and Oskarsson 1994; Médard et al. 2008). Compared to the Iron-Wüstite (IW) buffer (Frost 1991), these oxygen fugacity conditions at 15 kbar correspond to IW+1 at 1450 °C and IW at 2000 °C, within uncertainties which are estimated as ± 0.3 log units (Médard et al. 2008).

Solid state reaction synthesis

Citrate-based sol-gel precursors were prepared as described by Cinibulk (1998). The initial gel was formed by completely and sequentially dissolving in ethanol, under reflux, the appropriate amounts of aluminum nitrate $Al(NO_3)_3 \cdot 9H_2O$, magnesium nitrate $Mg(NO_3)_2 \cdot 6H_2O$, citric acid $HO_2CCH_2COHCOOHCH_2CO_2H \cdot H_2O$ (2 mole per 1 mole of Al) and calcium acetate $Ca(C_2H_3O_2)_2 \cdot H_2O$. Finally titanium isopropoxide $Ti[OCH(CH_3)_2]_4$ was added together with ethylene glycol $C_2H_6O_2$ (1 mol to every 1 mol of nitrates). The mixture was allowed to reflux (~ 82 °C) for 6 h, producing a pale yellow transparent sol, which, in case it turned turbid, could be cleared with the addition of nitric acid HNO_3 (0.2 mol per 1 mol of Ti-isopropoxide, Yoldas 1986). Small aliquots of the sol (~ 10-20 ml) were then heated up to 150 °C to promote gelification and subsequent polymerization; further heating to ~ 200 °C resulted in the removal of all the solvents, leaving a yellowish resin. Firing the resin up to ~ 600 °C removes all organics, giving an amorphous material, in which the cations are, ideally, uniformly dispersed on an atomistic scale throughout the

sample. This material was pressed into 1/2" pellets and heated to temperatures up to 1550 °C either in air (log fO_2 = -0.5) or under reducing conditions at log fO_2 = -11.0 (IW-2.5) using a gas-mixing furnace in which the oxygen fugacity is controlled by a CO/CO_2 flux (Table 1). The run products consisted of hibonite single crystals up to 90 μm in size (Fig. 2), except for gel0 (with composition of pure hibonite, $CaAl_{12}O_{19}$) whose crystals had sizes smaller than 10 μm and therefore could not be analyzed by means of single crystal XRD, thus X-ray powder diffraction was used instead.

SEM-EMPA characterization

The chemical compositions of hibonites were measured with a JEOL JXA-8200 electron microprobe (EMPA), fully-automated with five crystals and five wavelength dispersive spectrometers. The polished samples were coated with about 10 nm of amorphous carbon to avoid charging of the surface and studied at acceleration voltages of 15 kV and probe currents between 15 and 20 nA, measuring for 10 sec the pre- and post-peak backgrounds and 20 sec on the peak position. The analytical standards used for the calibration of the energy positions of the analyzed elements were: MgO for Mg, Al_2O_3 for Al, $MnTiO_3$ for Ti, wollastonite for Ca and enstatite for Si. Also Fe has been probed, however, its signal was below detection limit for all samples. For each specimen 20 to 40 points were measured and averaged (Table 2).

Optical spectroscopy

Optical spectra were obtained for gel6-1 and gel6-3 samples using a Bruker IFS20 Fourier Transform (FT) spectrometer with polychromatic beam from a tungsten source modulated using a Michelson interferometer and equipped with a quartz beam splitter for UV/Vis measurements. The measurements were performed in the range from 10000 to 25000 cm^{-1} accumulating up to 800 scans per spectrum in order to enhance the signal to noise ratio. Double polished thin sections were

prepared with chips from gel6-1 and gel6-3 run products and polarized spectra were obtained from crystals oriented with the *c* axis perpendicular to the direction of propagation of the light beam, i.e. parallel to the glass slide plane, in order to have the *c* axis parallel to the polarization direction, *E*. The orientations of hibonite crystals were determined by means of conoscopic methods (Raith et al., 2012) using a petrographic microscope. No signal above the background was visible for gel6-1 which was synthesized in air (log fO_2 = -0.5), however a strong absorption was observed for the crystals of sample gel6-3 synthesized at a log$f$ (O_2) = -11 (Fig. 3), indicating that a large portion of Ti in this hibonite is present as Ti^{3+} as discussed below.

X-ray powder diffraction data collection and analysis

X-ray powder diffraction was used for all synthetic runs for phase identification (Table 1). Diffraction patterns were collected in the 2θ range between 6 and 110 ° on a Philips X'Pert Pro diffractometer operating in reflection mode with Co $K\alpha_1$ monochromated radiation, using 0.03 ° step size and 1.8 °/min scan speed; Si NIST SRM 640c material was added to the powdered samples as internal standard. Rietveld refinements were carried out using the program suite EXPGUI (Toby 2001) based on the refinement algorithm GSAS (Larson and Von Dreele 2004). Refinements of the unit-cell parameters of all phases present in the run product were performed using the structural models from Bermanec et al. (1996), Oetzel and Heger (1999), Sasaki et al. (1987) and Grimes et al. (1983) for hibonite, corundum, Ca-Ti perovskite and spinel, respectively.

The unit-cell parameters of the end-member hibonite, gel0, determined by means of XRPD, a = 5.55822(4) Å, c = 21.9048(2) Å resulting in a volume cell of 586.060(7) $Å^3$, were used as an end-member reference, since we could not obtain any single crystal structural refinement of this sample due to the small size of its crystals.

Single crystal X-ray data collection and structure refinements

Hibonite single crystals were chosen for XRD characterization on the basis of their size, morphology and optical properties. A preliminary data set was collected on a 4-circle κ-geometry Xcalibur diffractometer equipped with CCD detector and monochromatic Mo Kα radiation. The crystals showing strong diffraction intensities were subsequently measured on a Huber SMC9000 4-circle diffractometer equipped with point detector and Mo Kα. The crystals yielding Bragg reflections with full width at half maximum (FWHM) smaller than 0.12 ° were further analyzed. Accurate unit-cell parameters were measured on the Huber diffractometer using the 8-position centering procedure (King and Finger 1979; Angel and Finger 2010) on more than ten selected independent reflections. The measurements and the subsequent least square refinement to calculate the symmetry constrained unit-cell parameters were performed with the software SINGLE04 (Angel and Finger 2010) and are reported in Table 3. Complete datasets of diffracted intensities for the selected crystals were measured on the Xcalibur diffractometer at room temperature with optimized number of frames with ω-scan (in one case combined with φ-scan) using 0.5 ° scan width. Data reduction and integration were performed using the CrysAlisPro software (Agilent Technologies 2012), which also includes the packages used for analytical absorption correction (Clark and Reid 1995) and empirical multi-scan correction (ABSPACK, Agilent Technologies 2012).

The structural refinements were carried out on squared structure factors ($F_{o/c}^2$) adopting the scattering curves for neutral atoms published on the International Tables for X-ray Crystallography (Hahn 2005) and using the program suite WinGx (Farrugia 1999) based on the refinement algorithm SHELX (Sheldrick 2008). All the refinements were performed in the space group $P6_3/mmc$ (N° 194) assuming a model for pure hibonite end-member based on the atomic coordinates proposed by Bermanec et al. (1996). Atomic coordinates and anisotropic thermal factors were refined for all samples, as well as an overall scale factor and a 2-term weighing scheme. The Fourier difference

maps were evaluated for each dataset in order to estimate the possible location of Ti in the structure of hibonite. Due to the high concentration of Ti in the crystals of gel6-1 and gel6-3, a significant residual electron density was observed at the M4 site, a trigonally distorted octahedron occurring in face-sharing pairs. After refining the Ti occupancy into the M4 site, another peak in the Fourier map appeared at the M2 site, a trigonal bipyramid. After this observation a structural model having Ti in both the M2 and the M4 sites was used to refine the structure of all the other samples, even for those whose Ti concentration was too low to give appreciable peaks in the Fourier difference maps, i.e. HBMT5 and gel4-1. The sum of the occupancies of Ti and Al on the same site has been constrained to be unitary and the coupled atoms were forced to have the same fractional coordinates and thermal factors; however the occupancy of Ti at these two sites has not been constrained. Data collections and refinements details, as well as atomic and displacement parameters are reported in Table 3 and 4, respectively.

Further structural analyses were performed considering the parameters describing distortions of coordination polyhedra, i.e. octahedral angle variance (OAV), as defined by Robinson et al. (1971) which were calculated using the software XtalDraw (Downs and Hall-Wallace 2003).

RESULTS AND DISCUSSION

The crystal chemistry of hibonite

The synthetic methods and conditions for the single crystals analyzed in this study are reported in Table 1; the expected nominal compositions are indicated together with the main phases detected by XRPD and the color of synthetic hibonite crystals. The average chemical compositions measured by EMPA on several crystals are listed in Table 2, where the total amount of Ti is calculated as TiO_2. The corresponding chemical formulae are calculated normalizing the cation numbers to 19 O.

Tables 1 and 2 also include the sample gel0, corresponding to polycrystalline pure end-member

hibonite. The run products obtained from the sol-gel precursors have a homogeneous composition, as revealed by the small deviations between EMPA analyses performed on several spots for each sample. The absence of zoning is also confirmed by SEM back scattered electron (BSE) imaging of all polished samples, see Fig. 2 as an example. Microprobe analyses of the sample prepared from oxide mixture (HBMT5) yield compositions with standard deviations similar to those of samples prepared by the sol-gel method. The unit-cell parameters obtained for each single crystal and those obtained from XRPD on the corresponding bulk sample agree very well, e.g. the volume cell for the sample gel6-3 obtained from XRPD is 604.10(4) $Å^3$ (compare with Table 3). The grain size of hibonite seems to be related to the concentration of doping elements (i.e. Ti and Mg, Table 3): larger crystals are produced at higher concentrations of Ti and Mg.

The composition of synthesized hibonite crystals is clearly different from the nominal composition of the starting materials (compare Table 1 and 2). The measured chemical formulae are closer to the nominal values for samples with low Ti-Mg content (HBMT5 and gel4-1). The samples with high Ti-Mg content have compositions that deviate from the nominal ones because Ti and Mg are also accommodated in the spinel and Ca-Ti-perovskite phases, also present in the run products (Table 1). Most of the samples have a Ti:Mg ratio that is close to 1:1, suggesting that the coupled substitution $2Al^{3+} = Ti^{4+} + Mg^{2+}$ is the major incorporation mechanism for Ti and Mg in hibonite. At low oxygen fugacity (gel6-3), the hibonite structure takes up more Ti, resulting in a small excess of Ti with respect to Mg, most likely because more reducing conditions favor the substitution of Ti^{3+} according to an $Al^{3+} = Ti^{3+}$ substitution. The presence of Ti^{3+} in gel6-3 is confirmed by the strong absorption band observed in the UV/Vis spectrum for this sample (Fig. 3). As demonstrated by Ihinger and Stolper (1986), this absorption band at 715 nm is uniquely attributed to the presence of Ti^{3+} and results in the blue color of hibonite. It was not possible to collect absorption spectra for

sample HBMT5, however these hibonite crystals are also blue in color (Table 1), suggesting the presence of trivalent Ti.

Effect of Ti-Mg incorporation on the unit-cell parameters

The unit-cell volume of the studied hibonites varies linearly with the concentration of Ti_{tot} + Mg (Fig. 4, Table 3); the solid line drawn on Fig. 4 is a linear fit through our data, which gives the following empirical relationship: $V = 8.21(3) \cdot (Ti_{tot} + Mg)_{a.p.f.u.} + 586.06(1)$. An increase of the unit-cell volume is consistent with an expansion of the oxygen framework as a consequence of the substitution of Al^{3+} (0.535 Å) with larger cations such as Mg^{2+} (0.720 Å), Ti^{4+} (0.605 Å) and Ti^{3+} (0.67 Å). The data reported in the literature generally lie above our trend; for pure end-member hibonite the unit-cell volumes reported by Hofmeister et al. (2004) and Utsunomiya et al. (1988) are 0.35 % and 0.70 % greater than the unit-cell volume obtained for the end-member hibonite synthesized in this study (gel0). This discrepancy may be due to the different synthesis procedures, which can give rise to varying degrees of non-stoichiometry affecting the unit-cell parameters, as well as to the accuracy in the centering of Bragg reflections, which can result in systematic errors. In the case of our samples, we have observed that the unit-cell parameters measured by means of XRPD are in good agreement with those obtained from the 8-positions centering method. The most outlying data point is that from Bermanec et al. (1996), reporting a cell volume 1.5 % larger than that described by our regression line, likely due to the presence of REE in this natural hibonite. In fact, the sample studied by Nagashima et al. (2010), being an unusually REE-free terrestrial hibonite, is in good agreement with our regression.

Effect of Ti-Mg incorporation on the hibonite structure

The occupancy of Ti has been refined both at the M2 and the M4 sites; the overall Ti concentration that can be calculated from the refined occupancies is in very good agreement with the EMPA measurements (Table 2 and 4). The variation of the M4-O bond distances as a function of Ti content is shown in Fig. 5. In contrast to what is reported by Nagashima et al. (2010), the distance M4-O5 does not seem to be influenced by the Ti substitution. The difference between M4-O5 and M4-O3 bond lengths increases as reported by Nagashima et al. (2010) simply because the M4-O3 bond length increases, as shown in Fig. 5. The change in M4-O3 bond length is due to the repulsion of the highly charged Ti atoms (mostly present as Ti^{4+}) and their consequent displacement from the central position of the polyhedron along the *c* axis. This displacement can be visualized by plotting the variation of the M4-M4 distance with respect to the Ti content (Fig. 6). For our synthetic samples, we observe that with increasing amount of Ti the M4-M4 distance increases. Note, however, that this distance is clearly smaller for gel6-3. This is likely due to the fact that this sample contains a larger amount of Ti^{3+} with respect to the other samples and as a consequence the repulsion between the M4 cations is weaker. The hibonites from Madagascar (Bermanec et al. 1996; Hofmeister et al. 2004) show a larger M4-M4 distance with respect to the trend represented by our samples; however this is not surprising given their complex chemistry. More puzzling are the differences between our samples and the hibonite studied by Nagashima et al. (2010), which has a much simpler chemical formula. However, this is possibly only an apparent discrepancy because the Ti content ($Ti_{a.p.f.u.}$ = 0.52) reported as EMPA analysis in Nagashima et al. (2010) is smaller than that calculated from the M2 and M4 site occupancies ($Ti_{a.p.f.u.}$ =0.61), listed in their XRD data. This would correspond to about 1 wt% more of TiO_2 in the formula of hibonite by Nagashima et al. (2010). Considering this larger amount of Ti, their data point is in better agreement with our results.

315 There also is some evidence of Ti occupying the M2 site. The axial (M2-O1) and equatorial
316 (M2-O3) bond distances are not clearly dependent on the Ti concentration; however we observe a
317 correlation between the displacement factor along the *c* axes, $M2_{U33}$ (Table 4), and the site
318 occupancy factor (*s.o.f.*) for Ti at the M2 site (Fig. 7). This displacement factor can be interpreted as
319 a measure of the cationic disorder in the trigonal bipyramid due to the different charge of
320 substituting cations. An increasing amount of Ti substituting for Al into the M2 site corresponds to
321 an enlargement of the displacement factor $M2_{U33}$. It appears, however, that $M2_{U33}$ remains that of
322 pure hibonite for small Ti occupancies at the M2 site. This plateau of displacement factor is similar
323 to the plateau of transition temperature or transition pressure (Salje et al. 1991; Hayward and Salje,
324 1996; Carpenter et al. 1999, 2009; Boffa Ballaran et al. 2000) that can be observed when a second
325 component of a solid solution is added into the structure of the other end-member. Change in the
326 transition point, or, in this case, in the displacement parameter occurs only once the microscopic
327 strain fields around the impurity atoms start to overlap. The magnitude of the plateau is therefore a
328 reflection of the magnitude of the local strain fields around the substituted Ti atoms. Since a visible
329 change in $M2_{U33}$ can be observed only for samples which have more than 0.3 – 0.4 $Ti_{a.p.f.u.}$ (Table 2
330 and 4), we can estimate that the strain fields around each Ti atom begins to overlap at a Ti-Ti
331 separation of about 1-2 unit cells. The significant difference of $M2_{U33}$ between our sample gel6-3
332 containing Ti^{3+} and the terrestrial hibonite from Nagashima et al. (2010), supposedly containing
333 only Ti^{4+} (Fig. 7) may therefore be due to smaller microscopic strain fields around the Ti^{3+} atoms as
334 well as to a weaker repulsion because of its smaller charge.
335 Due to the very low difference in the scattering factors of Al^{3+} and Mg^{2+} (the two cations are
336 isoelectronic), it was not possible to directly locate the position of Mg and thus the refinements were
337 carried out without considering this cation. However, there is a clear correlation between the
338 concentration of Mg in hibonite obtained from the EMPA and the M3-O tetragonal bond distance

(Fig. 8). We observe an elongation of the M3-O bond distance as a function of Mg content and we, therefore, can confirm that indeed divalent cations occupy the M3 site as suggested by Bermanec et al. (1996) and Nagashima et al. (2010). The variation of the average M3-O bond length with Mg content fits the following regression through our data: $d_{M3\text{-}O} = 0.065(3) \cdot Mg_{a.p.f.u.} + 1.800(2)$, where 1.800(2) is the extrapolated tetrahedral bond distance of pure hibonite. This value is in good agreement with the tetrahedral distances reported by Hofmeister et al. (2004) and Utsunomiya et al. (1988).

Substitution of Ti and Mg also affects the polyhedra which are occupied only by Al. In particular the site M1 becomes more irregular as a function of Mg content because of the expansion of the tetrahedron M3 which is connected to M1 through the bridging oxygen O4. This is clearly seen in the increase of the octahedral angle variance (OAV, Table 4), which is a measure of the distortion of the 6-fold coordination environment; i.e. the closer the OAV is to zero, the more regular the octahedron is. The M5 site instead is sandwiched between the layers where Ti and Mg are substituting (Fig. 1). As a result of the individual M5-O bond variations driven by the substitution in the adjacent sites, the M5 octahedron tends to become more regular as the substitution of Ti and Mg occurs into the structure of hibonite (Table 4).

IMPLICATIONS

The simple chemistry of the samples synthesized in this study allows us to exclusively determine the effect of Mg and Ti substitution on the hibonite structure. Ti clearly occupies both M4 and M2 sites (Figs. 6 and 7). At low oxygen fugacities we observe a detectable amount of Ti^{3+}, with a clear effect on the M4-M4 distance which deviates from the linear trend described by samples containing mainly Ti^{4+} (Fig. 6). The presence of a plateau effect in the change of the M2 displacement parameter with Ti substitution (Fig. 7) gives an idea of the magnitude of the microscopic strain

363 fields around the Ti atoms which appear to be similar to the strain fields inferred when Fe^{2+} atoms
364 are substituted by Mg into the grunerite structure (Boffa Ballaran et al. 2000) or for dopant atoms in
365 oxide perovskites (Carpenter et al. 2009).
366 The hibonites synthesized in this study have chemical compositions comparable to that of meteoritic
367 samples. Knowing the exact coordination of the Ti atoms is fundamental for quantifying the Ti^{3+}
368 /Ti^{4+} ratio in hibonite, as has been attempted in several studies aimed to give better insights on the
369 oxygen fugacity conditions in the solar nebula during formation and evolution of CAIs. These
370 studies have used UV/visible (Ihinger and Stolper 1986), ESR (Becket et al. 1988), EELS (Giannini
371 et al. 2011) and Xanes spectroscopy (Doyle et al. 2011) and have so far given only qualitative
372 results due to the fact that the coordination of Ti was based on simple assumptions. Chemical and
373 structural information as reported in this study provide strong constraints on the Ti distribution and
374 therefore can be used to quantify the spectroscopic result.
375

376 **ACKNOWLEDGMENTS**

377 The authors thank Hans Keppler for providing help in performing the spectroscopic measurements.
378 The research project was founded by the Deutsche Forschungsgemeinschaft through the priority
379 program1385 and the Leibniz program under the grants BO 2550 4-1, BO 2550 4-2, LA830-14, and
380 LA830-15 (to Boffa Ballaran T. and Langenhorst F.). We thank the two anonymous reviewers and
381 Rhian Jones for constructive comments.
382

383 **REFERENCES CITED**

384 Agilent Technologies (2012) CrysAlisPro Software system, Agilent Technologies UK Ltd., Oxford,
385 UK, Xcalibur/SuperNova CCD system.

386 An, L., Chan, H.M., and Soni, K.K. (1996) Control of calcium hexaluminate grain morphology in
387 in-situ toughened ceramic composites. Journal of Materials Science 31, 3223–3229.
388 Angel, R.J., and Finger, L.W. (2010) SINGLE: a program to control single-crystal diffractometers.
389 Journal of Applied Crystallography 44, 247–251.
390 Beckett, J., Live, D., Tsay, F., Grossman, L., and Stolper, E. (1988) Ti^{3+} in meteoritic and synthetic
391 hibonite. Geochimica et Cosmochimica Acta 52, 1479–1495.
392 Bermanec, V., Holtstam, D., Sturman, D., Criddle, A.J., Back, M.E., and Scavnicar, S. (1996)
393 Nezilovite, a new member of the magnetoplumbite group, and the crystal chemistry of
394 magnetoplumbite and hibonite. Canadian Mineralogist 34, 1287–1297.
395 Boffa Ballaran, T., Angel, R.J., and Carpenter, M.A. (2000) High-pressure transformation behavior
396 of the cummingtonite-grunerite solid solution. European Journal of Mineralogy 12, 1195-1213.
397 Boyd, F.R., and England, J.L. (1960) Apparatus for phase-equilibrium measurements at pressures
398 up to 50 kilobars and temperatures up to 1750°C. Journal of Geophysical Research 65, 741–748.
399 Carpenter, M.A., Boffa Ballaran, T., and Atkinson, A.J. (1999) Microscopic strain, local structural
400 heterogeneity and the energetics of silicate solid solutions. Phase transitions 69, 95-109.
401 Carpenter, M.A., McKnight, R.E.A., Howard, C.J., Zhou, Q., Kennedy, B.J., and Knight K. (2009)
402 Characteristic length scale for strain fields around impurity cations in perovskites. Physical review
403 B 80, 214101.
404 Cinibulk, M.K. (1995) Thermal-stability of some hexaluminates at 1400 °C. Journal of Materials
405 Science Letters 14, 651–654.
406 Cinibulk, M.K. (1998) Effect of precursors and dopants on the synthesis and grain growth of
407 calcium hexaluminate. Journal of the American Ceramic Society 81, 3157–3168.
408 Clark, R.C., and Reid, J.S. (1995) The analytical calculation of absorption in multifaceted crystals.
409 Acta Crystallographica Section A Foundations of Crystallography 51, 887–897.

Dominguez, C., Chevalier, J., Torrecillas, R., Gremillard, L., and Fantozzi, G. (2001) Thermomechanical properties and fracture mechanisms of calcium hexaluminate. Journal of the European Ceramic Society 21, 907–917.

Downs, R.T., and Hall-Wallace, M. (2003) The American Mineralogist crystal structure database. American Mineralogist 88, 247–250.

Doyle, P., Berry, A., Schofield, P., Mosselmans, F., Smith, A., Scholl, A., and Young, T. (2011) The oxidation state of Ti in synthetic and meteoritic hibonite. Mineralogical Magazine 75, 778.

Farrugia, L. (1999) WinGX suite for small-molecule single-crystal crystallography. Journal of Applied Crystallography 32, 837–838.

Frost, B.R. (1991) Introduction to oxygen fugacity and its petrologic importance. Reviews in Mineralogy and Geochemistry 25, 1–9.

Geiger, C., Kleppa, O., Mysen, B., Lattimer, J., and Grossman, L. (1988) Enthalpies of formation of $CaAl_4O_7$ and $CaAl_{12}O_{19}$ (hibonite) by high temperature, alkali borate solution calorimetry. Geochimica Et Cosmochimica Acta 52, 1729–1736.

Giannini, M., Ballaran, T.B., Langenhorst, F., and Bischoff, A. (2011) TEM-EELS study of titanium oxidation state in meteoritic hibonites. Meteoritics & Planetary Science 46, A77–A77.

Grimes, N.W., Thompson, P., and Kay, H.F. (1983) New symmetry and structure for spinel. Proceeding Royal Society of London A 386, 333–345.

Grossman, L., and Clark Jr., S. (1973) High-temperature condensates in chondrites and the environment in which they formed. Geochimica et Cosmochimica Acta 37, 635–649.

Hahn, T. (2005) International Tables for Crystallography, Space-Group Symmetry, John Wiley & Sons.

Hayward, S., and Salje, E.K.H. (1996) Displacive phase transition in anorthoclase: The "plateau effect" and the effect of T1-T2 ordering on the transition temperature. American Mineralogist 81, 1332-1336.

Hinton, R., Davis, A., Scatenawachel, D., Grossman, L., and Ddraus, R. (1988) A chemical and isotopic study of hibonite-rich refractory inclusions in primitive meteorites. Geochimica et Cosmochimica Acta 52, 2573–2598.

Hofmeister, A.M., Wopenka, B., and Locock, A.J. (2004) Spectroscopy and structure of hibonite, grossite, and $CaAl_2O_4$: Implications for astronomical environments. Geochimica et Cosmochimica Acta 68, 4485–4503.

Ihinger, P.D., and Stolper, E. (1986) The color of meteoritic hibonite: an indicator of oxygen fugacity. Earth and Planetary Science Letters 78, 67–79.

Ireland, T.R. (1990) Presolar isotopic and chemical signatures in hibonite-bearing refractory inclusions from the Murchison carbonaceous chondrite. Geochimica et Cosmochimica Acta 54, 3219–3237.

Jakobsson, S., and Oskarsson, N. (1994) The system C-O in equilibrium with graphite at high pressure and temperature: An experimental study. Geochimica et Cosmochimica Acta 58, 9–17.

King, H.E., and Finger, L.W. (1979) Diffracted beam crystal centering and its application to high-pressure crystallography. Journal of Applied Crystallography 12, 374–378.

Larson, A. C., and Von Dreele, R. B. (2004) General Structure Analysis System (GSAS), Los Alamos National Laboratory: LAUR 86-748.

Maaskant, P. (1980) Hibonite and Coexisting Zoisite and Clinozoisite in a Calc-Silicate Granulite from Southern Tanzania. Mineralogical Magazine 43, 995–1003.

Mateika, D., and Laudan, H. (1979) Czochralski growth of barium hexaaluminate single crystals. Journal of Crystal Growth 46, 85–90.

Médard, E., McCammon, C.A., Barr, J.A., and Grove, T.L. (2008) Oxygen fugacity, temperature reproducibility, and H_2O contents of nominally anhydrous piston-cylinder experiments using graphite capsules. American Mineralogist 93, 1838–1844.

Momma, K., and Izumi, F. (2011) VESTA 3 for three-dimensional visualization of crystal, volumetric and morphology data. Journal of Applied Crystallography 44, 1272-1276.

Nagashima, M., Armbruster, T., and Hainschwang, T. (2010) A temperature-dependent structure study of gem-quality hibonite from Myanmar. Mineralogical Magazine 74, 871–885.

Nakamura, T.M., Sugiura, N., Kimura, M., Miyazaki, A., and Krot, A.N. (2007) Condensation and aggregation of solar corundum and corundum-hibonite grains. Meteoritics and Planetary Science 42, 1249-1265.

Oetzel, M., and Heger, G. (1999) Laboratory X-ray powder diffraction: a comparison of different geometries with special attention to the usage of the Cu Kα doublet. Journal of Applied Crystallography 32, 799–807.

Raith, M.M., Raase, P., and Reinhardt, J. (2012) Guide to thin section microscopy, 127 p. Mineralogical Society of America, Chantilly.

Robinson, K., Gibbs, G.V., and Ribbe, P.H. (1971) Quadratic elongation: a quantitative measure of distortion in coordination polyhedra. Science 172, 567–570.

Sasaki, S., Prewitt, C.T., Bass, J.D., and Schulze, W.A. (1987) Orthorhombic perovskite $CaTiO_3$ and $CdTiO_3$: structure and space group. Acta Crystallographica Section C Crystal Structure Communications 43, 1668–1674.

Salje, E.K.H., Bismayer, U., Wruck, B., and Hensler, J. (1991) Influence of lattice imperfections on the transition temperature of structural phase transitions - the plateau effect. Phase Transitions 35, 61-74.

Simon, S.B., Davis, A.M., Grossman, L., and McKeegan, K.D. (2002) A hibonite-corundum inclusion from Murchison: A first generation condensate from the solar nebula. Meteoritics and Planetary Science 37, 533-548.

Sheldrick, G.M. (2008) A short history of SHELX. Acta Crystallographica Section A Foundations of Crystallography 64, 112–122.

Toby, B.H. (2001) EXPGUI, a graphical user interface for GSAS. Journal of Applied Crystallography 34, 210–213.

Ulianov, A., Kalt, A., and Pettke, T. (2005) Hibonite, $Ca(Al,Cr,Ti,Si,Mg,Fe^{2+})_{12}O_{19}$, in granulite xenoliths from the Chyulu Hills volcanic field, Kenya. European Journal of Mineralogy 17, 357–366.

Utsunomiya, A., Tanaka, K., Morikawa, H., Marumo, F., and Kojima, H. (1988) Structure refinement of $CaO{\cdot}6Al_2O_3$. Journal of Solid State Chemistry 75, 197–200.

Yoldas, B.E. (1986) Hydrolysis of titanium alkoxide and effects of hydrolytic polycondensation parameters. Journal of Materials Science 21, 1087–1092.

FIGURES CAPTIONS

Figure 1. Crystal structure of hibonite showing the coordination polyhedra and the repetitive blocks. The figure was generated using the software VESTA (Momma and Izumi, 2011).

Figure 2. SEM-BSE image of gel6-1 sample. Light grey =hibonite (hib), dark grey = spinel (sp), white = Ca-Ti-perovskite (pv) , black = voids.

Figure 3. Absorption spectra of samples gel6-1 synthesized in air (dotted line) and gel6-3 synthesized at an oxygen fugacity of $\log fO_2 = -11$ (solid line). The strong absorption band at 715 nm of gel6-3 indicates that part of Ti in hibonite is present as Ti^{3+}.

Figure 4. Unit-cell volume of hibonites as a function of the sums of the transition metal cations substituting for Al. Vertical diamonds = single crystals from this study; horizontal diamond = gel0; open symbols = literature data. The solid line indicates a fit through the data points of this study (R^2 = 1.00) according to the expression $V = 8.21(3) \cdot (Ti_{tot} + Mg)_{a.p.f.u.} + 586.06(1)$.

Figure 5. Bond distances M4-O5 and M4-O3 as a function of the sum of trivalent and tetravalent cations, in the case of this study exclusively Ti, substituting for Al. Symbols as in Figure 4. The solid line indicates a fit through the data points for this study ($R^2 = 0.96$) according to the expression $d_{M4\text{-}O3} = 0.42(2) \cdot (Ti_{tot})_{a.p.f.u.} + 1.961(2)$ while the horizontal dashed line is a guide to the eyes drawn through the average of our data in order to show that the M4-O5 distance is independent of cation substitution.

Figure 6. Inter-atomic distance M4-M4 as a function of the sum of trivalent and tetravalent cations, in the case of this study exclusively Ti, substituting for Al. Symbols as in Figure 4. The solid line indicates a fit through the data points for this study, excluding gel6-3 which deviates from the linear trend due to the presence of Ti^{3+}: $d_{M4\text{-}M4} = 0.117(3) \cdot (Ti_{tot})_{a.p.f.u.} + 2.584(2)$, ($R^2 = 1.00$).

Figure 7. Displacement factor U_{33} for the M2 site as a function of the corresponding refined site occupancy factor, *s.o.f.*, of Ti. Solid diamonds = this study, open symbols = literature data. The solid line indicates a fit through the data points for this study ($R^2 = 0.95$), excluding gel6-3: $M2_{U33} = 0.17(5) \cdot (Ti_{s.o.f.})_{a.p.f.u.}$. The dotted line indicates a possible plateau at 0.008(3) $Å^2$ which represents the displacement factor for pure hibonite.

Figure 8. Bond distances M3-O as a function of the sum of divalent cations substituting for Al, in the case of this study exclusively Mg. Symbols as in Figure 4. The solid line indicates a fit through the data points for this study ($R^2 = 0.99$) according to the expression $d_{M3\text{-}O} = 0.065(3) \cdot Mg_{a.p.f.u.} + 1.800(2)$.

526 **TABLES**

527 **Table 1.** Synthetic methods, conditions and run products for hibonite samples.

Sample	Method[§]	Temp. [°C]	log fO_2	time [h]	Nominal composition of hibonite	Main products[*]	Color of hibonite[#]
HBMT5	PC	1450 2000	-7.6 -4.9	12 1.5	$CaAl_{11.25}Ti_{0.42}Mg_{0.33}O_{19}$	hib	blue
gel4-1	SG	1550	-0.5	15	$CaAl_{11.4}Ti_{0.40}Mg_{0.20}O_{19}$	hib	white
gel6-1	SG	1550	-0.5	15	$CaAl_{8.00}Ti_{2.00}Mg_{2.00}O_{19}$	hib + sp + pv	white
gel6-3	SG	1550	-11	15	$CaAl_{8.00}Ti_{2.00}Mg_{2.00}O_{19}$	hib + sp + pv	blue
gel0	SG	1550	-0.5	15	$CaAl_{12.00}O_{19}$	hib	white

[§]PC = piston cylinder, SG = sol-gel; [*]detected as > 5 $\%_{wt}$ from XRPD: hib = hibonite, pv = Ca-Ti-perovskite, sp = spinel; [#]color of the recovered pellets after firing at high temperature: while the bulk color of samples synthesized in air appears white, the individual single crystals are colorless.

528

529

530
531 **Table 2.** Chemical composition of hibonite crystals determined by EMPA; one-sigma standard
532 deviations are given in brackets. For each sample 20 to 40 points were measured and averaged.

	HBMT5	**gel4-1**	**gel6-1**	**gel6-3**	**gel0**
			Oxides wt%		
CaO	8.51(7)	8.40(6)	8.21(7)	8.19(8)	8.64(6)
Al_2O_3	86.3(4)	86.7(2)	75.4(2)	72.4(5)	91.1(5)
MgO	1.9(1)	1.28(2)	5.27(7)	5.7(1)	==
TiO_2	4.3(3)	3.4(1)	11.0(1)	13.8(2)	==
Tot.	101.0(2)	99.7(2)	99.9(3)	100.2(4)	99.8(5)
			Cations per formula unit, normalized to 19 oxygen atoms		
Ca	1.01(2)	1.01(2)	1.00(2)	1.00(2)	1.03(2)
Al	11.30(4)	11.47(2)	10.14(2)	9.75(4)	11.98(2)
Mg	0.31(3)	0.21(2)	0.90(2)	0.97(3)	==
Ti*	0.36(4)	0.28(2)	0.94(2)	1.18(3)	==

***Total amount of Ti calculated as Ti^{4+}.

533

534 **Table 3.** Details for data collection and refinements from single crystal XRD measurements

535 performed on hibonite.

	HBMT5	gel4-1	gel6-1	gel6-3
Crystal size [mm]	0.175x0.115x0.045	0.06x0.04x0.01	0.19x0.17x0.09	0.135x0.095x0.03
***a* [Å]**	5.5778(6)	5.5711(7)	5.6071(4)	5.6192(4)
***c* [Å]**	21.9523(7)	21.9448(8)	22.0653(4)	22.0944(5)
***V* [Å^3]**	591.5(1)	589.9(1)	600.80(8)	604.18(8)
Scan type	φ-ω scan	ω scan	ω scan	ω scan
θ_{max} [°]	63.66	64.2	72.79	72.67
Reflections	12489	10949	16667	2997
Unique reflections	441	442	615	596
R_{int} [%]	3.63	9.47	4.50	3.17
R_s [%]	3.29	5.37	4.14	5.15
R_1 [%]	2.78	3.82	4.05	3.99
wR_2 [%]	7.71	9.66	9.88	9.99
Number of parameters	44	44	44	44

536

537

538 **Table 4.** Refined atomic coordinates, displacement parameters and angle variations for the analyzed
539 hibonites.

Site	Wyck.†	Sym.#	Ref.*	HBMT5	gel4-1	gel6-1	gel6-3
A	2*d*	$\bar{6}m2$	*x*	⅓	⅓	⅓	⅓
			y	⅔	⅔	⅔	⅔
			z	¾	¾	¾	¾
			U_{eq}	0.0213(2)	0.0212(4)	0.0272(3)	0.0288(4)
M1	2*a*	$\bar{3}m$	*x*	0	0	0	0
			y	0	0	0	0
			z	0	0	0	0
			U_{eq}	0.0066(3)	0.0070(4)	0.0058(3)	0.0062(3)
			OAV	14.22	11.93	22.69	24.23
M2	4*e*	3*m*.	*x*	0	0	0	0
			y	0	0	0	0
			z	0.2414(2)	0.2407(2)	0.2414(2)	0.2411(2)
			U_{33}	0.017(3)	0.006(4)	0.022(3)	0.023(2)
			U_{eq}	0.0097(9)	0.006(1)	0.010(1)	0.013(1)
			s.o.f.	0.10(1)	0.04(1)	0.13(2)	0.18(2)
M3	4*f*	3*m*.	*x*	⅓	⅓	⅓	⅓
			y	⅔	⅔	⅔	⅔
			z	0.02785(4)	0.02783(6)	0.02731(5)	0.02727(5)
			U_{eq}	0.0069(2)	0.0074(3)	0.0081(2)	0.0091(3)
M4	4*f*	3*m*.	*x*	⅓	⅓	⅓	⅓
			y	⅔	⅔	⅔	⅔
			z	0.19019(3)	0.19036(6)	0.18895(4)	0.18912(3)
			U_{eq}	0.0063(3)	0.0060(4)	0.0060(3)	0.0065(2)
			s.o.f.	0.115(6)	0.07(1)	0.32(1)	0.413(8)
M5	12*k*	.*m*.	*x*	0.16823(5)	0.16835(8)	0.16748(6)	0.16751(7)
			y	0.33646(9)	0.3367(2)	0.3350(1)	0.3350(1)
			z	0.89148(2)	0.89138(4)	0.89247(3)	0.89273(3)

			U_{eq}	0.0064(2)	0.0068(3)	0.0063(2)	0.0065(2)
			OAV	32.49	33.58	29.02	29.19
O1	4*e*	3*m*.	*x*	0	0	0	0
			y	0	0	0	0
			z	0.14956(9)	0.1493(2)	0.1503(1)	0.1504(1)
			U_{eq}	0.0076(4)	0.0071(7)	0.0078(4)	0.0081(5)
O2	4*f*	3*m*.	*x*	⅓	⅓	⅓	⅓
			y	⅔	⅔	⅔	⅔
			z	0.94399(9)	0.9444(2)	0.9421(1)	0.9420(1)
			U_{eq}	0.0082(4)	0.0094(7)	0.0083(4)	0.0091(5)
O3	6*h*	*mm*2	*x*	0.1808(2)	0.1808(3)	0.1808(2)	0.1802(2)
			y	0.3616(3)	0.3616(5)	0.3617(4)	0.3603(4)
			z	¼	¼	¼	¼
			U_{eq}	0.0091(4)	0.0090(5)	0.0093(4)	0.0106(4)
O4	12*k*	.*m*.	*x*	0.1542(1)	0.1545(2)	0.1524(2)	0.1518(2)
			y	0.3083(2)	0.3090(4)	0.3048(3)	0.3036(3)
			z	0.05254(6)	0.05222(9)	0.05323(6)	0.05325(6)
			U_{eq}	0.0083(3)	0.0085(4)	0.0092(3)	0.0094(3)
O5	12*k*	.*m*.	*x*	0.50359(9)	0.5036(2)	0.5041(1)	0.5048(1)
			y	0.0072(2)	0.0072(4)	0.0082(3)	0.0096(3)
			z	0.14956(6)	0.14941(9)	0.14983(6)	0.14986(6)
			U_{eq}	0.0076(3)	0.0077(4)	0.0070(3)	0.0080(3)
$(Ti_{tot})_{a.p.f.u.}$ [**]				0.33(2)	0.18 (3)	0.78(3)	1.01(2)

[†]Wyckoff symbol; [#]Site symmetry; [*]Refined values: U_{33} [Å^2], U_{eq} [Å^2] and *s.o.f.* = site occupancy factor; the OAV=octahedral angle variance is expressed in deg; [**]Ti content per formula unit calculated from Ti *s.o.f.* for M2 and M4 sites.

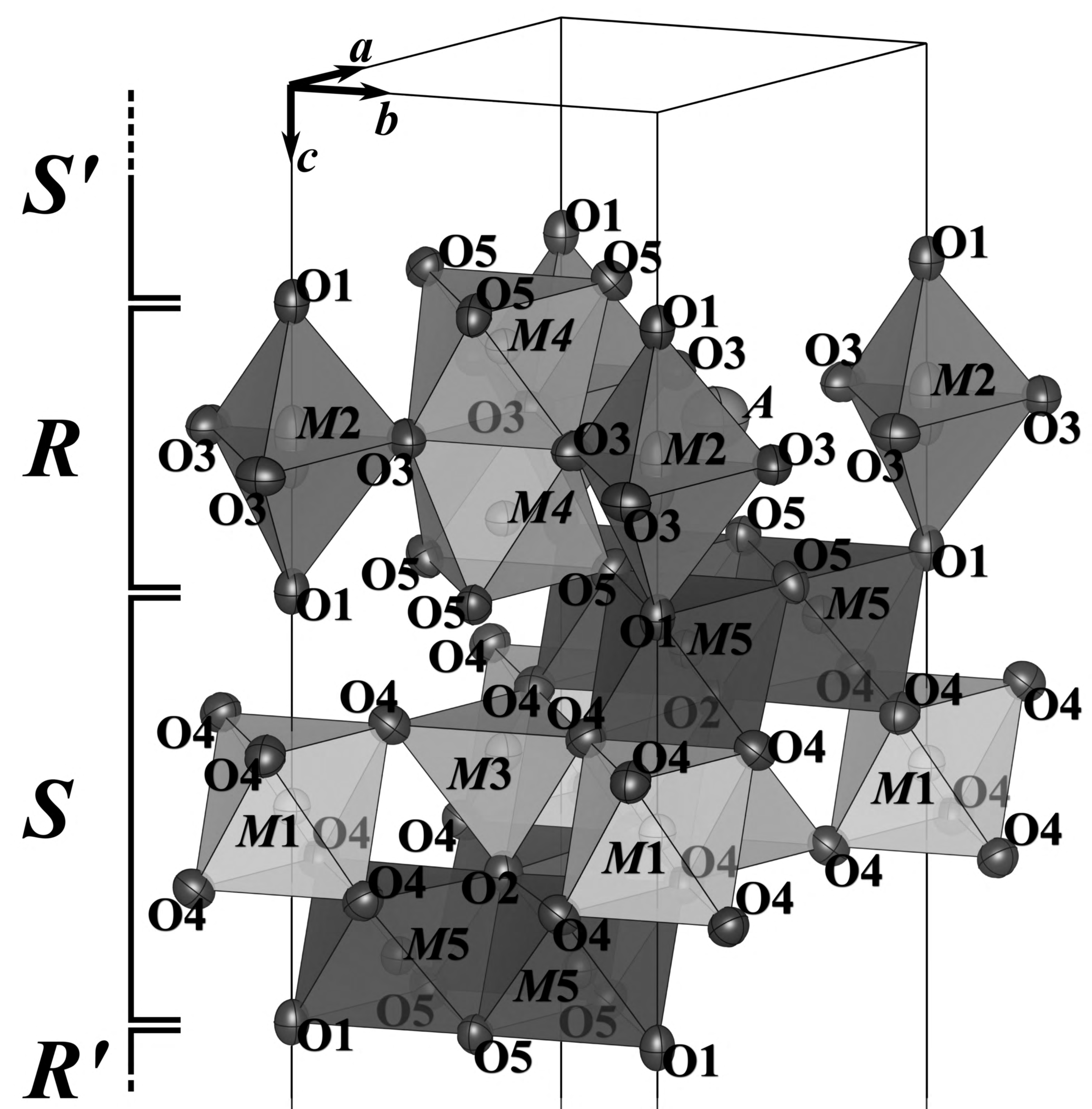
a
b
c
S'
R
S
R'
O1
O5
M4
O3
M2
A
M5
O4
O2
M3
M1

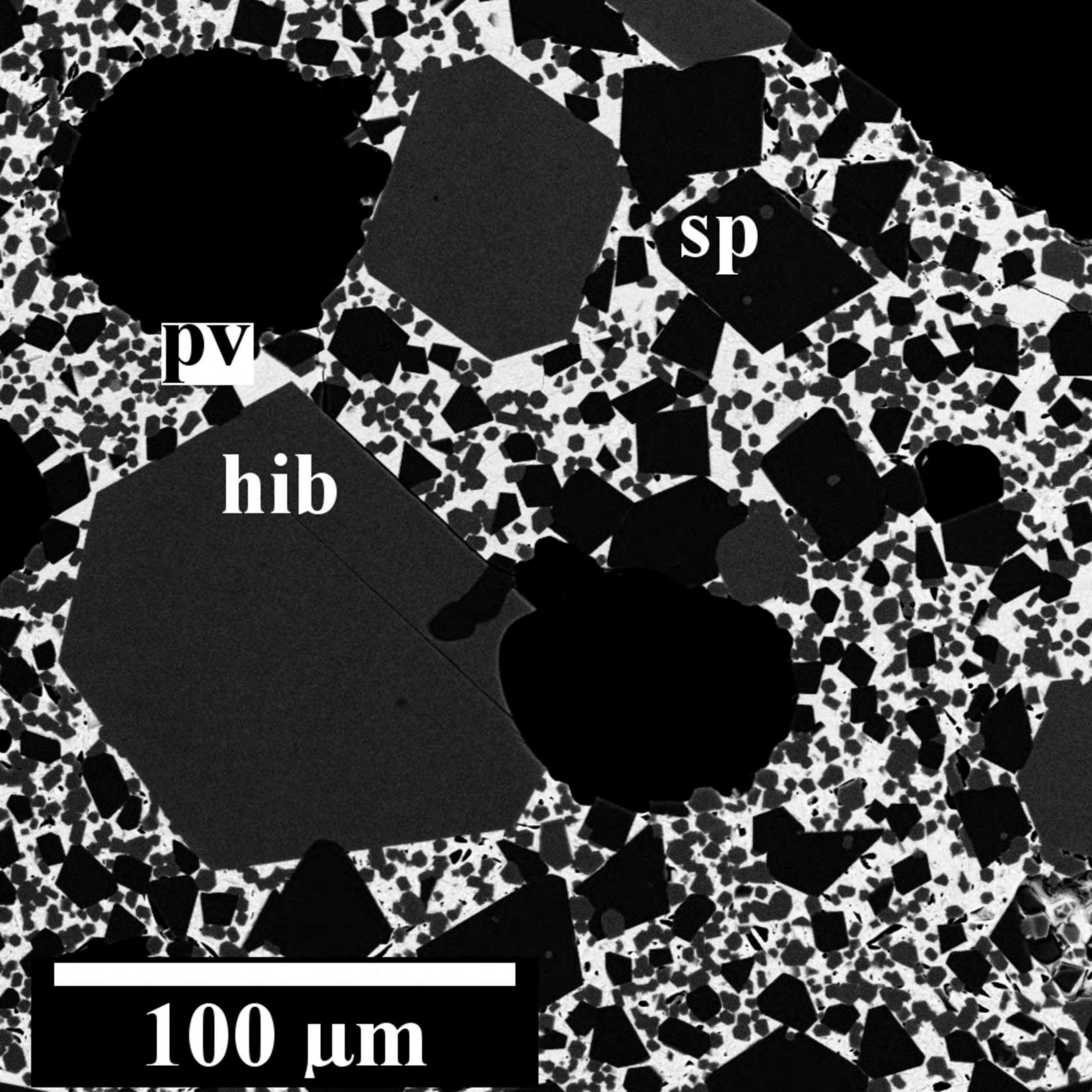
sp
pv
hib
100 µm

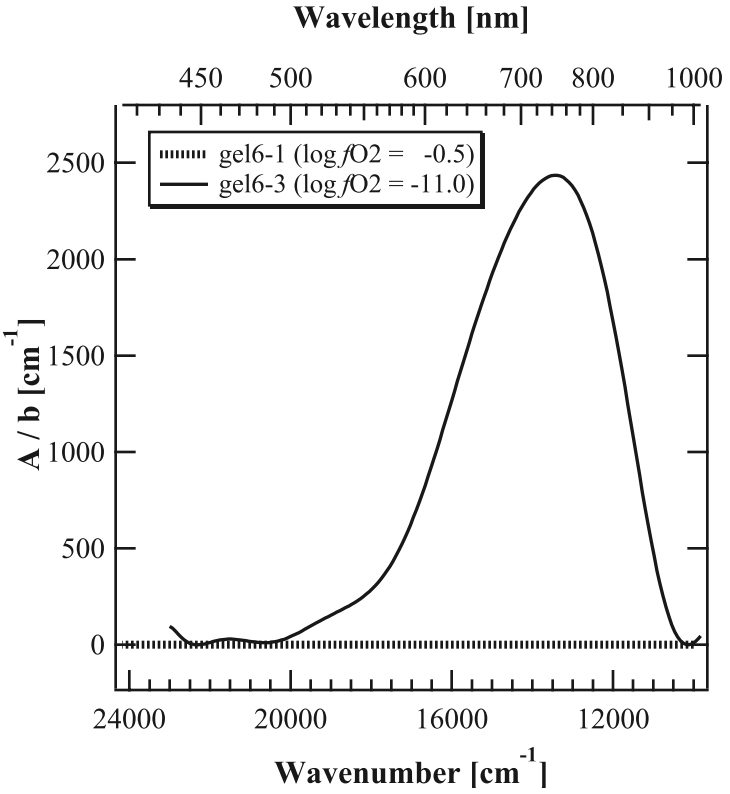
Wavelength [nm]
450
500
600
700
800
1000
gel6-1 (log fO2 = -0.5)
gel6-3 (log fO2 = -11.0)
2500
2000
1500
1000
500
0
A / b [cm-1]
24000
20000
16000
12000
Wavenumber [cm-1]

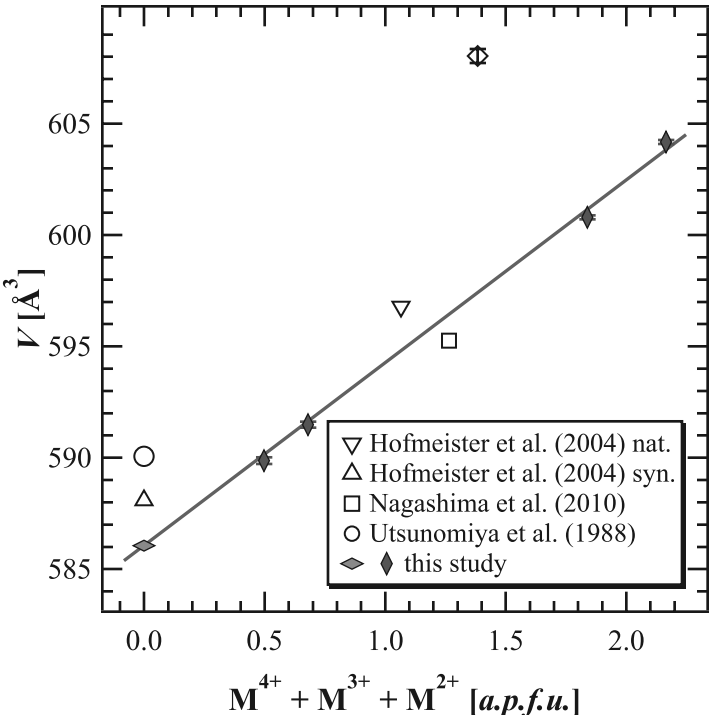
605
600
595
590
585
V [Å3]
0.0
0.5
1.0
1.5
2.0
M4+ + M3+ + M2+ [a.p.f.u.]
Hofmeister et al. (2004) nat.
Hofmeister et al. (2004) syn.
Nagashima et al. (2010)
Utsunomiya et al. (1988)
this study

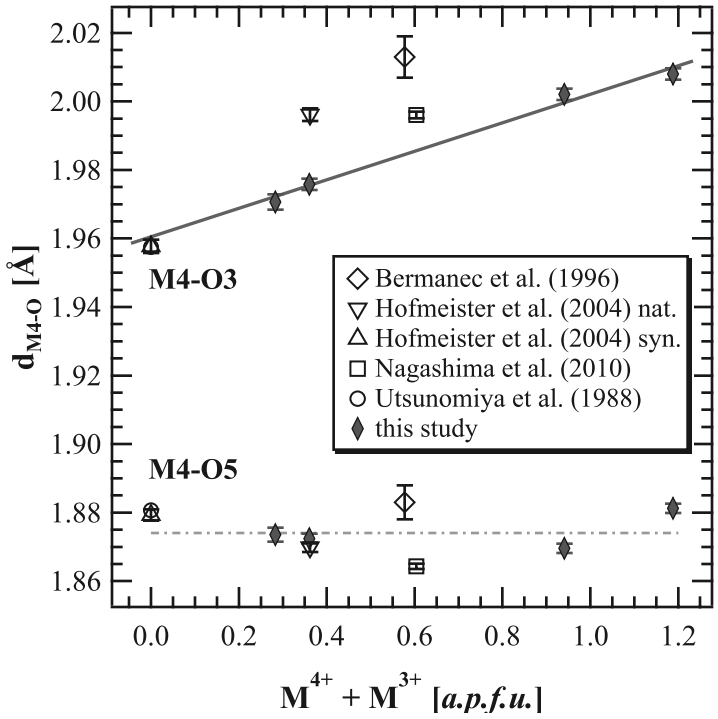
2.02
2.00
1.98
1.96
1.94
1.92
1.90
1.88
1.86
d_{M4-O} [Å]
M4-O3
M4-O5
Bermanec et al. (1996)
Hofmeister et al. (2004) nat.
Hofmeister et al. (2004) syn.
Nagashima et al. (2010)
Utsunomiya et al. (1988)
this study
0.0
0.2
0.4
0.6
0.8
1.0
1.2
$M^{4+} + M^{3+}$ [*a.p.f.u.*]

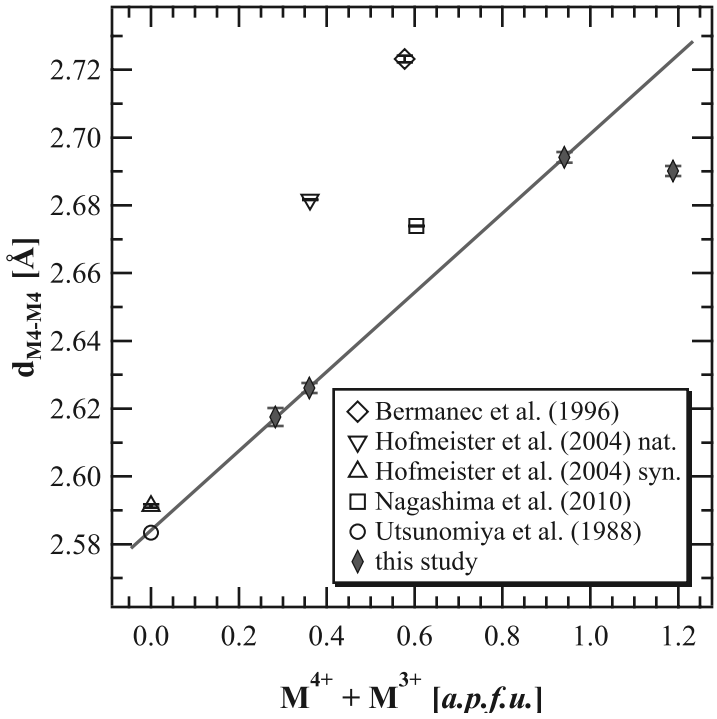
2.72
2.70
2.68
2.66
2.64
2.62
2.60
2.58
d_{M4-M4} [Å]
0.0
0.2
0.4
0.6
0.8
1.0
1.2
$M^{4+} + M^{3+}$ [*a.p.f.u.*]
Bermanec et al. (1996)
Hofmeister et al. (2004) nat.
Hofmeister et al. (2004) syn.
Nagashima et al. (2010)
Utsunomiya et al. (1988)
this study

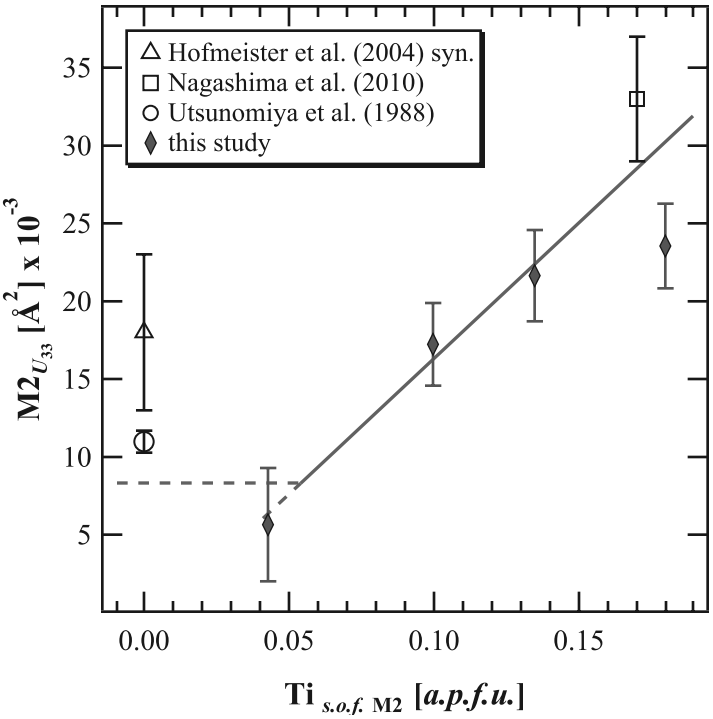
Hofmeister et al. (2004) syn.
Nagashima et al. (2010)
Utsunomiya et al. (1988)
this study
35
30
25
20
15
10
5
0.00
0.05
0.10
0.15
M2$_{U_{33}}$ [Å^2] x 10^{-3}
Ti $_{s.o.f.\ M2}$ [*a.p.f.u.*]

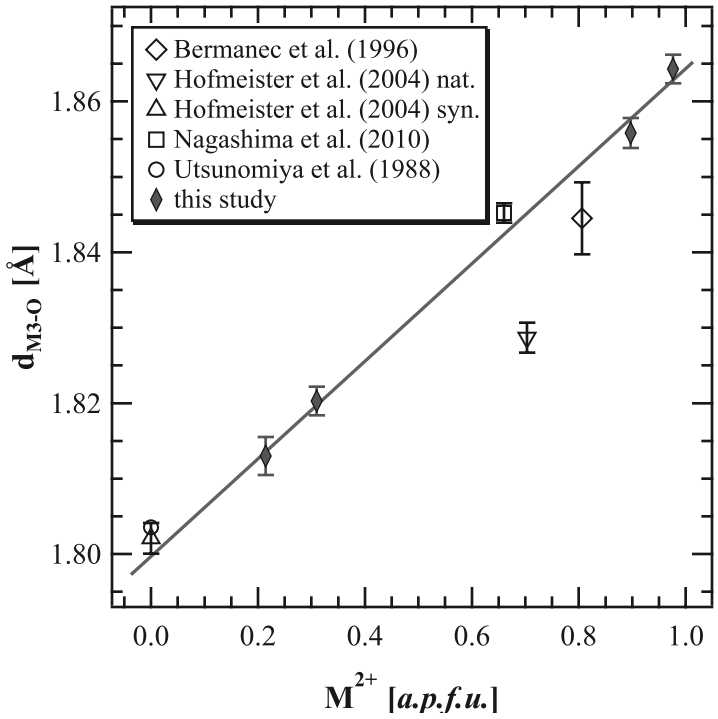
Bermanec et al. (1996)
Hofmeister et al. (2004) nat.
Hofmeister et al. (2004) syn.
Nagashima et al. (2010)
Utsunomiya et al. (1988)
this study
1.80
1.82
1.84
1.86
0.0
0.2
0.4
0.6
0.8
1.0
d_M3-O [Å]
M2+ [a.p.f.u.]